

See discussions, stats, and author profiles for this publication at: <https://www.researchgate.net/publication/266569045>

# Elemental Fingerprinting of Materials with Sensitivity at the Atomic Limit

ARTICLE *in* NANO LETTERS · OCTOBER 2014

Impact Factor: 13.59 · DOI: 10.1021/nl5030613 · Source: PubMed

---

CITATIONS

4

---

READS

53

## 8 AUTHORS, INCLUDING:



[Marvin Cummings](#)

Argonne National Laboratory

8 PUBLICATIONS 27 CITATIONS

[SEE PROFILE](#)



[D. Rosenmann](#)

Argonne National Laboratory

91 PUBLICATIONS 742 CITATIONS

[SEE PROFILE](#)



[Volker Rose](#)

Argonne National Laboratory

68 PUBLICATIONS 760 CITATIONS

[SEE PROFILE](#)

# Elemental Fingerprinting of Materials with Sensitivity at the Atomic Limit

Nozomi Shirato,<sup>†</sup> Marvin Cummings,<sup>†</sup> Heath Kersell,<sup>‡</sup> Yang Li,<sup>‡</sup> Benjamin Stripe,<sup>†</sup> Daniel Rosenmann,<sup>§</sup> Saw-Wai Hla,<sup>\*,‡,§</sup> and Volker Rose<sup>\*,†,§</sup>

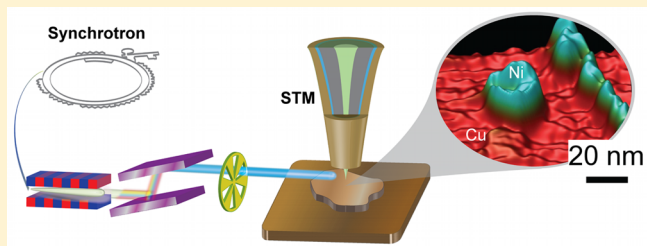
<sup>†</sup>Advanced Photon Source, Argonne National Laboratory, 9700 South Cass Ave, Argonne, Illinois 60439, United States

<sup>‡</sup>Nanoscale and Quantum Phenomena Institute, Physics & Astronomy Department, Ohio University, Athens, Ohio 45701, United States

<sup>\*</sup>Center for Nanoscale Materials, Argonne National Laboratory, 9700 South Cass Ave., Argonne, Illinois 60439, United States

## S Supporting Information

**ABSTRACT:** By using synchrotron X-rays as a probe and a nanofabricated smart tip of a tunneling microscope as a detector, we have achieved chemical fingerprinting of individual nickel clusters on a Cu(111) surface at 2 nm lateral resolution, and at the ultimate single-atomic height sensitivity. Moreover, by varying the photon energy, we have succeeded to locally measure photoionization cross sections of just a single Ni nanocluster, which opens new exciting opportunities for chemical imaging of nanoscale materials.



**KEYWORDS:** X-ray microscopy, chemical imaging, scanning tunneling microscopy, smart tips, synchrotron

The direct observation of chemical composition with high spatial contrast has been a long-standing goal for characterization of nanoscale materials. Since its development in the 1980s, scanning tunneling microscopy (STM) has become an indispensable tool for investigating structural, electronic and magnetic properties of materials down to the atomic scale.<sup>1–7</sup> However, albeit the undisputable success observed, STM has one major limitation: it is chemically blind. It cannot be used alone to directly fingerprint the elemental species at the surface, because tunneling electrons originate from states close to the Fermi energy and do not carry any chemical information. In contrast to the STM, X-ray microscopy is an excellent tool for the chemical characterization of materials, because the ionization energies of core level electrons constitute the fingerprints of the elements in the periodic table. However, even with the best synchrotron X-ray microscopes available to date, direct chemical imaging cannot be reached below a spatial limit of about 10 nm.<sup>8–11</sup> Thus, an instrument that combines these two robust methods, synchrotron radiation and scanning probe microscopy,<sup>12–16</sup> has a great potential to resolve both topography and chemical composition simultaneously. Because synchrotron X-ray scanning tunneling microscopy (SX-STM) combines two powerful techniques, all the capabilities of STM such as atomic scale imaging, single atom spectroscopy, and atomic manipulations<sup>1–7,17</sup> can now be performed at synchrotron beamlines that enable a wide variety of X-ray measurements<sup>8–11</sup> including X-ray photoelectron spectroscopy, near-edge X-ray absorption fine structure, small-angle X-ray scattering, X-ray absorption spectroscopy, X-ray tomography and so on. The SX-STM technique also promises magnetic contrast in

nanostructures combined with elemental contrast.<sup>18</sup> Nevertheless, single atom imaging with elemental contrast has been advancing in scanning transmission electron microscopy (STEM).<sup>19</sup> Both SX-STM and STEM have their advantages and disadvantages. For instance, in STEM the sample has to be subjected to primary electrons with energies much higher than the photoelectrons generated in SX-STM, which could adversely impact the integrity of the sample. On the other hand, STEM is extremely useful to probe interfaces with atomic structures, while SX-STM will be mainly used to probe surface chemical elements, although the bulk chemical compositions can also be measured by spectroscopic techniques. Thus, STEM and SX-STM are complementary to each other and the scientists will now be equipped with atomic scale elemental and chemical characterization suits that will enable critical advances in materials, chemical, and biological sciences.

For this experiment, we have used beamline ID26 at the Advanced Photon Source,<sup>20</sup> where an undulator device at the synchrotron storage ring serves as the X-ray source (Figure 1a), and the photon energy is selected by a double-crystal monochromator. After the X-rays have passed through a beam chopper operating at a frequency of about 3 kHz, the beam illuminates the tip/sample junction in our synchrotron X-ray scanning tunneling microscope under grazing incident conditions (~3 degrees with respect to the surface normal). The beam chopper switches the X-ray illumination on and off and

**Received:** August 8, 2014

**Revised:** September 21, 2014

**Published:** October 2, 2014



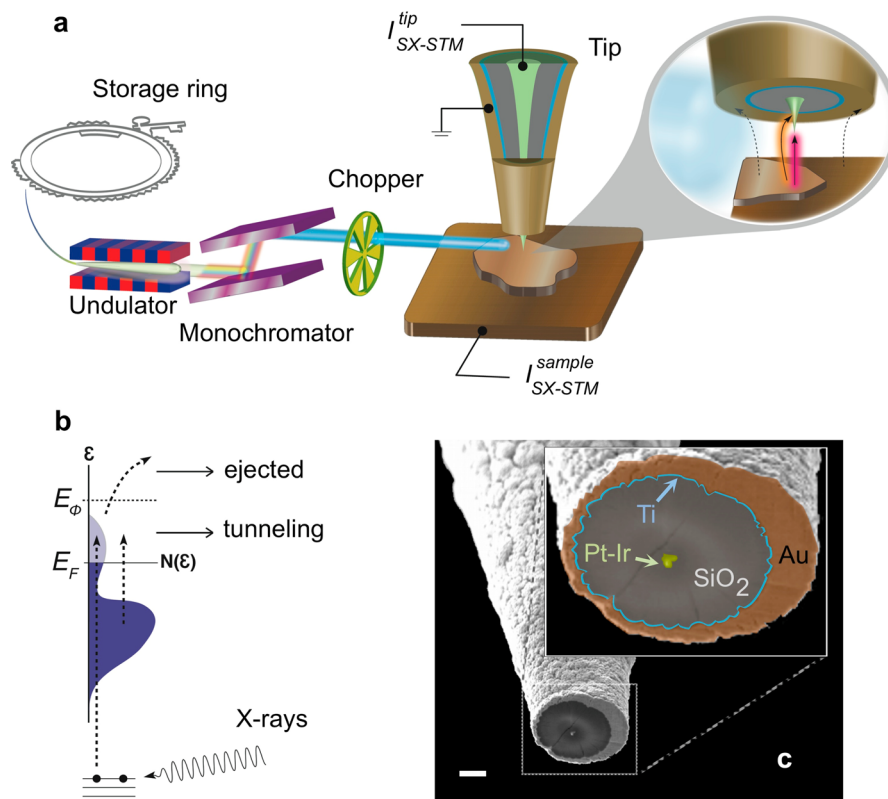


**Figure 1.** Concept of synchrotron X-ray scanning tunneling microscopy (SX-STM). (a) A monochromatic X-ray beam is steered into the tunnel junction of a scanning tunneling microscope. An undulator device at the electron storage ring serves as high-brilliance photon source. The X-rays pass through a beam chopper in order to enable lock-in detection of the X-ray induced tip current  $I_{\text{STM}}^{\text{tip}}$  and the sample current  $I_{\text{STM}}^{\text{sample}}$ . (b) Band structure schematic of the X-ray excitation process. X-rays tuned to a specific core level energy can excite primary core electrons and also secondary electrons to unoccupied levels close to the Fermi energy  $E_F$ , which then become available for tunneling. Furthermore, some electrons will have energies higher than the work function  $E_\Phi$ , and are consequently ejected from the sample. (c) Scanning electron micrograph of a nanofabricated coaxial “smart tip”, which enhances the signal detection. The Pt–Ir tip is shielded by an insulating  $\text{SiO}_2$  layer, which is covered by metallic Ti and Au films. The Au film is grounded to reduce background. Scale bar:  $1 \mu\text{m}$ .

provides the reference frequency for the lock-in detection of the X-ray induced currents (Supporting Information). The total currents

$$I_{\text{STM}}^{\text{tip}} = I_{\text{topo}} + I_{\text{X-ray}}^{\text{tip}}$$

and

$$I_{\text{STM}}^{\text{sample}} = I_{\text{topo}} + I_{\text{X-ray}}^{\text{sample}}$$

are detected at the tip and sample, respectively.  $I_{\text{topo}}$  refers to the conventional tunnel current, which is solely related to the sample topography, while  $I_{\text{X-ray}}^{\text{tip}}$  and  $I_{\text{X-ray}}^{\text{sample}}$  are the X-ray-induced currents measured at the tip and sample, respectively. The STM topographic signal,  $I_{\text{topo}}$ , is measured at the beam-off time, while the X-ray induced currents (chemical signals),  $I_{\text{X-ray}}^{\text{tip}}$  and  $I_{\text{X-ray}}^{\text{sample}}$ , are recorded at the beam-on time. The X-ray-induced currents consist of two contributions: X-ray-enhanced tunneling<sup>21</sup> and photoejected electrons<sup>22,23</sup> (Figure 1b).

To achieve a high spatial contrast in chemical imaging with SX-STM, it is necessary to overcome a number of hurdles. When a sample is illuminated with X-rays of a suitable energy, some core-level electrons and secondary electrons are excited to unoccupied levels close to Fermi energy  $E_F$ , while electrons that overcome the work function of the material  $E_\Phi$  are ejected from the sample. These photoejected electrons can arise from the entire illuminated sample area, which is about  $50 \times 700 \mu\text{m}^2$  in our experiment, and the tip can collect them. For a

high spatial contrast, localized detection of photoelectrons is vital and therefore insulator-coated tips with only a small opening at the tip apex have been previously used.<sup>24–26</sup> However, charging of the insulating layer by the photoelectrons can perturb the tunneling process in these tips. Thus, we use a new type of nanofabricated coaxial *smart tips*, which has an outer conducting shell on top of the insulating layer (Figure 1c and Supporting Information). Electrical grounding of the conducting shell prevents the undesired charging effects. Another obstacle is that the currents  $I_{\text{STM}}^{\text{tip}}$  and  $I_{\text{STM}}^{\text{sample}}$  measured at the beam-on time are generated by a convolution of the conventional tunnel current  $I_{\text{topo}}$  and the X-ray-excited components. Separation of  $I_{\text{topo}}$  from the X-ray-excited currents is essential to provide the correct topographic signal and thus, we use a recently developed topographic filter.<sup>27</sup>

The Cu(111) substrate crystal is cleaned by repeated cycles of sputtering with  $\text{Ar}^+$  ions and annealing inside the ultrahigh vacuum (UHV) system. A submonolayer ( $\sim 0.3$  mono layer) coverage of Ni is deposited onto the atomically clean surface at room temperature. The sample is then transferred to the STM scanner housed in the same UHV system. SX-STM measurements are performed with  $-1 \text{ V}$  sample bias and with a current set point of  $1 \text{ nA}$ . The synchrotron X-ray energy used for the experiment ranges from  $8$  to  $9 \text{ keV}$ , with a monochromatic photon flux density of about  $10^{13} \text{ photons s}^{-1} \text{ mm}^{-2}$ .

The SX-STM experiments were conducted at room temperature in UHV environment. A STM topography image (Figure 2a)

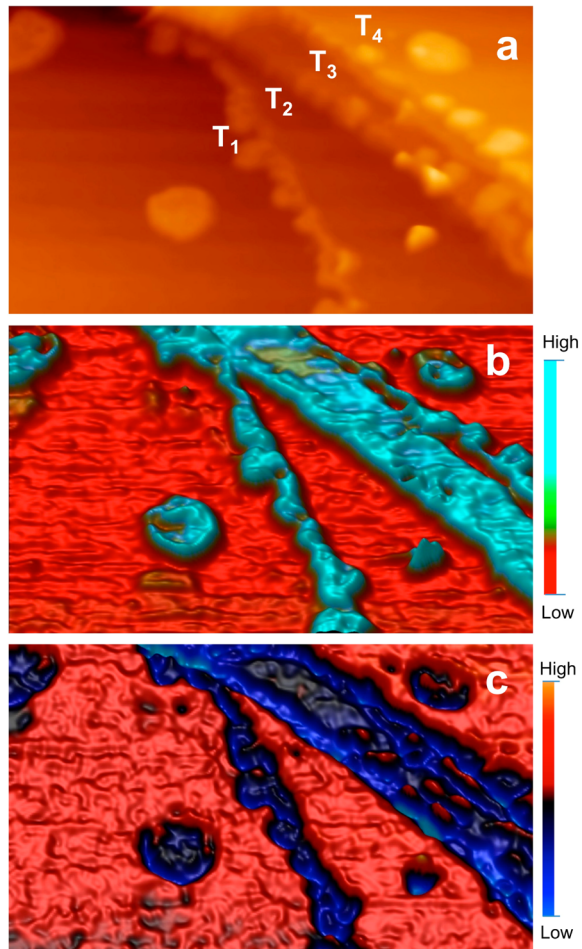


**Figure 2.** Nickel islands grown on Cu(111). (a) The conventional topography exhibits various Cu terraces (T<sub>1</sub>-T<sub>4</sub>) ( $190 \times 110 \text{ nm}^2$ ,  $-1 \text{ V}$ ,  $1 \text{ nA}$ ). (b) Chemical contrast  $I_{\text{X-ray}}^{\text{sample}}$  between Ni islands and Cu as obtained in the sample current channel with a photon energy of 8.55 keV. (c) Chemical contrast  $I_{\text{X-ray}}^{\text{tip}}$  observed simultaneously in the tip current channel. Images are 3D rendered to reflect the chemical height information.

recorded after the deposition of Ni on a clean Cu(111) surface shows nanosize Ni clusters located on the bare Cu surface as well as at the Cu step edges. Figure 2b presents the simultaneously measured sample photocurrent image,  $I_{\text{X-ray}}^{\text{sample}}$  using a photon energy of 8.55 keV (above the Ni absorption edge). Remarkably, all the Ni clusters are sharply contrasted as protrusions (enhanced current) from the Cu substrate background, indicating that we have achieved chemical contrast of Ni. Likewise, chemical contrast is also observed in the simultaneously measured tip photocurrent image,  $I_{\text{X-ray}}^{\text{tip}}$  (Figure 2c). Here, the Ni clusters appear as depressions (reduced current). This is because in our experiment electrons that arrive at the sample/tip generate a negative current, while electrons that leave the sample/tip give rise to a positive current signal. In the STM topography image (Figure 2a), the terraces T<sub>1</sub>, T<sub>2</sub>, T<sub>3</sub>, and T<sub>4</sub> appear similar and thus, one might assume that they are all Cu terminated. Interestingly, both chemical contrast images (Figure 2b and 2c) reveal that the terrace T<sub>3</sub> is actually formed by Ni. This highlights the strength and robustness of SX-STM for elemental identification.

The vital component in chemical identification using X-rays is the photoionization cross section of materials.<sup>28</sup> Generally,

atoms absorb X-rays sharply at their absorption edge energies that are characteristic of that atomic species and directly allow materials to be chemically fingerprinted. In conventional measurements, photoionization cross sections are obtained as an average over a large surface area and also by averaging over a substantial X-ray probing depth. To date, the photoionization cross section of an individual nanoparticle has yet to be determined. Here, we have successfully measured the local photoionization cross section of a single Ni cluster shown in Figure 3a. As revealed by an STM line scan in Figure 3b, this Ni cluster is  $\sim 20 \text{ nm}$  wide and just two atomic layer thick ( $\sim 0.33 \text{ nm}$  height).<sup>29</sup> In this measurement, the normalized Ni contrast obtained at the sample, i.e. the ratio of  $I_{\text{X-ray}}^{\text{sample}}$  on the island versus the Cu(111) substrate, is determined for photon energies between 8 and 9 keV. As expected, the Ni contrast exhibits a jump-wise increase when the photon energy exceeds the Ni absorption edge at 8.33 keV (Figure 3c, top). Likewise, the same behavior can be observed in the normalized Ni contrast measured at the tip as a rapid increase of the negative current (Figure 3c, bottom). This measurement clearly demonstrates the highly localized nature of the SX-STM technique and opens up new avenues of materials characterization at the nanoscale.

The jump of the photoionization cross section at the absorption edge has also been directly visualized. Shown in Figure 3d is a chemical image acquired at the photon energy of 8.25 keV. Since this image is obtained below the Ni K-edge energy of 8.33 keV, the Ni clusters as well as the Cu substrate produce almost the same current. Likewise, the Cu step does not produce any contrast, because both terraces are chemically identical. When the X-ray energy is raised to 8.55 keV, which is above the Ni K-edge, all the Ni clusters exhibit distinct contrast (Figure 3e). Remarkably, the rest of the surface including the monatomic Cu step remains flat at the level of the background noise.

Next, we turn our attention to determine the physical mechanisms that produce chemical contrast and the limit on the cluster thickness. Figure 4a shows a topographic image of Ni clusters on Cu(111) together with the corresponding chemical contrast images measured by the sample (Figure 4b) and the tip currents (Figure 4c). A small Ni cluster indicated with an arrow in Figure 4a is enlarged in Figure 4d, and the corresponding sample and tip chemical contrast images are shown in Figure 4, parts e and f, respectively. This Ni cluster is  $\sim 4 \text{ nm}$  wide and exhibits single-atomic height as determined from the STM topographic line profile (Figure 4g, bottom), while the larger Ni cluster next to it is two-atomic-layer thick. The pronounced chemical contrast of the small Ni cluster (Figures 4e and 4f) clearly demonstrate that chemical fingerprinting of materials is achievable down to an ultimate limit of single-atomic height. An interesting finding here is that both single and two-atomic-layer high Ni clusters exhibit the same intensity in the chemical contrast (Figure 4g, top, and Supporting Information). If photoejected electrons, i.e., electrons that overcome the work function of the material, dominated the observed chemical contrast, then the photocurrent should increase with the cluster thickness. Tunneling, however, is a local effect and sensitive only to the topmost layer of materials. Thus, the same height appearance in the chemical contrast of single and two-atomic-layer thick Ni clusters suggests that the observed chemical contrast is governed by tunneling of X-ray excited photoelectrons that originate from states between the Fermi level and the work function  $E_{\Phi}$ .

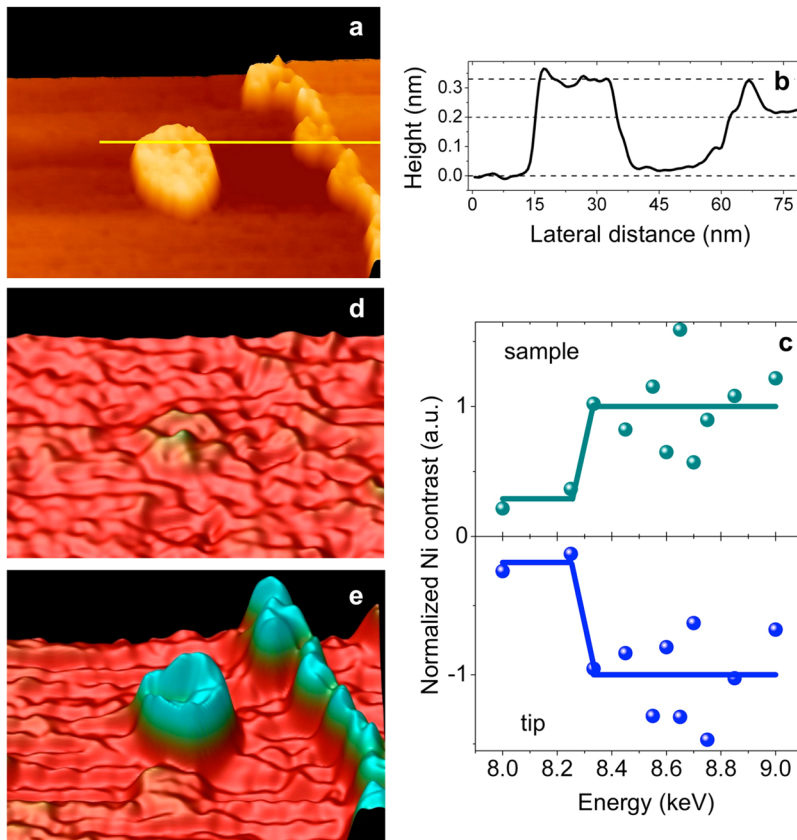


**Figure 3.** | Localized X-ray cross-section of a Ni island. (a) Perspective 3-D view of a STM topography scan ( $110 \times 60 \text{ nm}^2$ ,  $-1 \text{ V}$ ,  $1 \text{ nA}$ ). (b) Height profile of the line shown in the topography scan. (c) X-ray cross section of a single Ni island obtained from  $I_{X\text{-ray}}^{\text{sample}}$  (top) and  $I_{X\text{-ray}}^{\text{tip}}$  (bottom). (d) Sample current  $I_{X\text{-ray}}^{\text{sample}}$  does not provide chemical contrast, when the X-ray energy ( $E = 8.25 \text{ keV}$ ) is below the Ni K-edge ( $8.33 \text{ keV}$ ). (e) The Ni island on the Cu(111) terrace and islands along the Cu step edge become clearly visible for photon energies above the Ni K-edge, here  $E = 8.55 \text{ keV}$ .

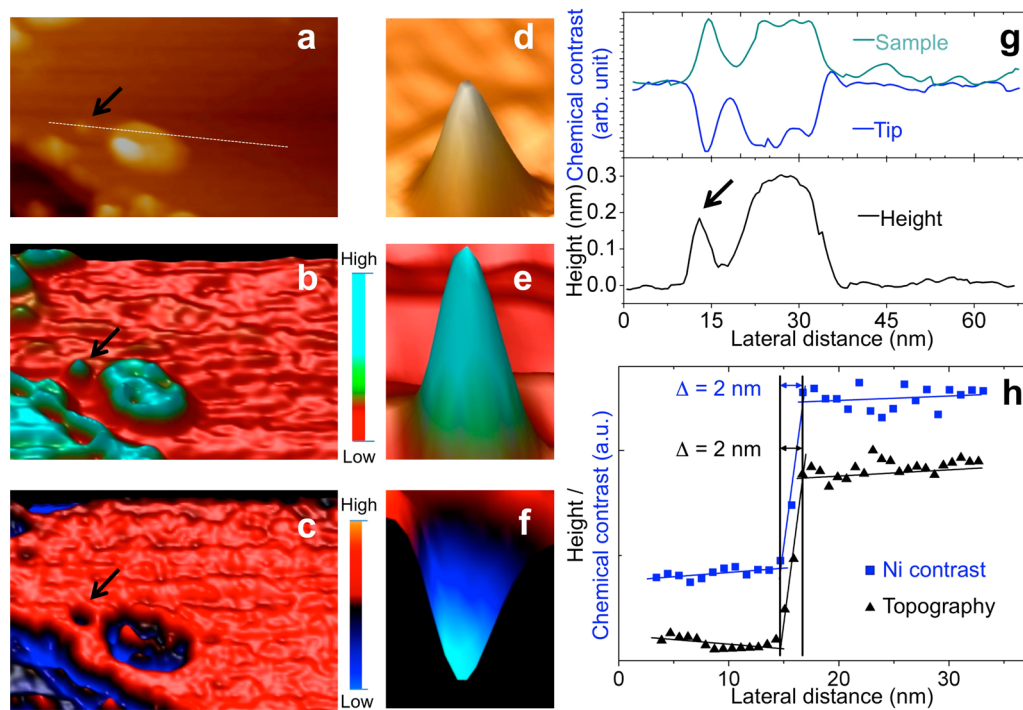


**Figure 4.** Spatial resolution of the chemical contrast. (a) STM topography scan ( $74 \times 60 \text{ nm}^2$ ,  $-1 \text{ V}$ ,  $1 \text{ nA}$ ). The arrow points to a small Ni cluster. (b) Chemical contrast in the sample current  $I_{X\text{-ray}}^{\text{sample}}$  at  $8.55 \text{ keV}$ . (c)  $I_{X\text{-ray}}^{\text{tip}}$  obtained simultaneously. (d) Topography zoom of the small Ni cluster and corresponding chemical images for (e)  $I_{X\text{-ray}}^{\text{sample}}$  and (f)  $I_{X\text{-ray}}^{\text{tip}}$ . (g) Height profile (bottom) of the line shown in the topography scan, and the chemical contrast (top) over the two adjacent Ni clusters measured at the sample and the tip. (h) Line profiles of a Ni cluster edge (black) and corresponding chemical contrast (blue) reveal the same lateral resolution,  $\Delta = 2 \text{ nm}$ .

To date, the record lateral resolution of SX-STM published in the literature is in the order of 10 nm.<sup>12,14</sup> In latter work, the lateral resolution discrepancy between the chemical and topographic line profiles across a surface structure is presented as the *spatial resolution*.<sup>12</sup> The lateral resolution of the STM tip used in our experiment is determined from the tip height profiles across a Ni cluster, and it is found to be  $\Delta = 2$  nm (Figure 4h). Remarkably, the lateral resolution of the corresponding chemical contrast profile also gives  $\Delta = 2$  nm. Thus, the discrepancy between the lateral resolution of the sample and the tip is 0 nm, which means the spatial limit of the chemical contrast in our measurement is exactly the topographic resolution. This further implies that atomic resolution in the chemical contrast could be achieved, if the topographic signal itself has atomic resolution.

Our findings suggest that localized influence of X-ray excited electron tunneling exceeds the contribution of photoejected electrons, and therefore the topmost atomic surface layer becomes vital in SX-STM measurements. Consequently, chemical contrast with atomic resolution is foreseeable at lower substrate temperatures. In the current study, the very low atomic corrugation height of Ni atoms and room temperature thermal noise hinder resolving of atomic structures inside the Ni clusters. However, this room temperature demonstration of obtaining chemical contrast down to the ultimate single-atomic height with 2 nm lateral resolutions has the distinct advantage that it is well suited for the needs of most physical, chemical, biological and nanomaterial applications. The availability of direct chemical contrast in STM has been a dream since the technique was developed, and this achievement is not only vital for material characterizations, but also opens up new avenues for studying novel emerging phenomena at the nanoscale.

## ■ ASSOCIATED CONTENT

### Supporting Information

Experimental information on separating photoexcited signals from topography, fabrication of coaxial metal/insulator/metal smart tips, and additional proof of single atom height chemical contrast. This material is available free of charge via the Internet at <http://pubs.acs.org>.

## ■ AUTHOR INFORMATION

### Corresponding Authors

<sup>\*</sup>(V.R.) E-mail: [vrose@anl.gov](mailto:vrose@anl.gov).

<sup>\*</sup>(S.-W.H.) E-mail: [shla@anl.gov](mailto:shla@anl.gov).

### Author Contributions

S.-W.H. and V.R. designed the experiment. D.R. fabricated smart tips. N.S., M.C., H.K., Y.L. D.R., S.-W.H., and V.R. carried out experiments. B.S. gave technical support. N.S., M.C., H.K., Y.L. S.-W.H. and V.R. conducted data analysis. All authors contributed to the writing/editing of the paper and overall scientific interpretation. All authors have given approval to the final version of the manuscript.

### Notes

The authors declare no competing financial interest.

## ■ ACKNOWLEDGMENTS

This work was funded by the Office of Science Early Career Research Program through the Division of Scientific User Facilities, Office of Basic Energy Sciences, U.S. Department of Energy, through Grant SC70705. Work at the Advanced Photon Source, the Center for Nanoscale Materials, and the Electron Microscopy Center was supported by the U.S. Department

of Energy, Office of Science, Office of Basic Energy Sciences, under Contract DE-AC02-06CH11357. H.K. and Y.L. acknowledge the support by the U.S. Department of Energy, Office of Science, Office of Basic Energy Sciences, Grant DE-FG02-02ER46012. The authors acknowledge engineering support by Curt Preissner and help with tip fabrication by Jon Hiller. The authors also thank the team of the CNM/APS nanoprobe for support at the beamline.

## ■ REFERENCES

- (1) Binnig, G.; Rohrer, H.; Gerber, Ch.; Weibel, E. *Phys. Rev. Lett.* **1983**, *50*, 120–123.
- (2) Liljeroth, P.; Swart, I.; Paavilainen, S.; Repp, J.; Meyer, G. *Nano Lett.* **2010**, *10*, 2475–2479.
- (3) Okada, Y.; Zhou, W.; Walkup, D.; Dhital, C.; Wilson, S. D.; Madhavan, V. *Nature Commun.* **2012**, *3*, 1158.
- (4) DiLullo, A.; Chang, S.-H.; Baadjii, N.; Clark, K.; Klöckner, J.-P.; Prosenc, M.-H.; Sanvito, S.; Wiesendanger, R.; Hoffmann, G.; Hla, S.-W. *Nano Lett.* **2012**, *12*, 3174–3179.
- (5) Yoshida, S.; Aizawa, Y.; Wang, Z.-H.; Oshima, R.; Mera, Y.; Matsuyama, E.; Oigawa, H.; Takeuchi, O.; Shigekawa, H. *Nat. Nanotechnol.* **2014**, *9*, 588–593.
- (6) Grill, L.; Rieder, K.-H.; Moresco, F.; Stojkovic, S.; Gourdon, A.; Joachim, Ch. *Nano Lett.* **2006**, *6*, 2685–2689.
- (7) Goler, S.; Coletti, C.; Tozzini, V.; Piazza, V.; Mashoff, T.; Beltram, F.; Pellegrini, V.; Heun, S. *J. Phys. Chem. C* **2013**, *117*, 11506–11513.
- (8) Ice, G. E.; Budai, J. D.; Pang, J. W. L. *Science* **2011**, *334*, 1234–1239.
- (9) Holt, M.; Harder, R.; Winarski, R.; Rose, V. *Annu. Rev. Mater. Res.* **2013**, *43*, 183–211.
- (10) Chao, W.; Harteneck, B. D.; Liddle, J. A.; Anderson, E. H.; Attwood, D. T. *Nature* **2005**, *435*, 1210–1213.
- (11) Zakharov, A. A.; Mikkelsen, A.; Andersen, J. N. *J. Electron Spectrosc. Relat. Phenom.* **2012**, *185*, 417–428.
- (12) Okuda, T.; Eguchi, T.; Akiyama, K.; Harasawa, A.; Kinoshita, T.; Hasegawa, Y.; Kawamori, M.; Haruyama, Y.; Matsui, S. *Phys. Rev. Lett.* **2009**, *102*, 105503.
- (13) Pilet, N.; Raabe, J.; Stevenson, S. E.; Romer, S.; Bernard, L.; McNeill, C. R.; Fink, R. H.; Hug, H. J.; Quitmann, C. *Nanotechnology* **2005**, *23*, 475708.
- (14) Saito, A.; Maruyama, J.; Manabe, K.; Kitamoto, K.; Takahashi, K.; Takami, K.; Yabashi, M.; Tanaka, Y.; Miwa, D.; Ishii, M.; Takagi, Y.; Akai-Kasaya, M.; Shin, S.; Ishikawa, T.; Kuwahara, Y.; Aono, M. *J. Synchrotron Radiat.* **2006**, *13*, 216–220.
- (15) Cummings, M. L.; Chien, T. Y.; Preissner, C.; Madhavan, V.; Diesing, D.; Bode, M.; Freeland, J. W.; Rose, V. *Ultramicroscopy* **2012**, *112*, 22–31.
- (16) Bechtel, H. A.; Muller, E. A.; Olmon, R. L.; Martin, M. C.; Raschke, M. B. *Proc. Nat. Acad. Sci.* **2014**, *111*, 7191–7196.
- (17) Hla, S. W. *Rep. Prog. Phys.* **2014**, *77*, 056502.
- (18) Rose, V.; Chien, T. Y.; Freeland, J. W.; Rosenmann, D.; Hiller, J.; Metlushko, V. *J. Appl. Phys.* **2012**, *111*, 07E304.
- (19) Krivanek, O. L.; Chisholm, M. F.; Nicolosi, V.; Pennycook, T. J.; Corbin, G. J.; Dellby, N.; Murfitt, M. F.; Own, C. S.; Szilagyi, Z. S.; Oxley, M. P.; Pantelides, S. T.; Pennycook, S. J. *Nature* **2010**, *464*, 571–574.
- (20) Winarski, R. P.; Holt, M. V.; Rose, V.; Fuesz, P.; Carbaugh, D.; Benson, C.; Shu, D.; Kline, D.; Stephenson, G. B.; McNulty, I.; Maser, J. *J. Synchrotron Radiat.* **2012**, *19*, 1056–1060.
- (21) Rose, V.; Wang, K.; Chien, T. Y.; Hiller, J.; Rosenmann, D.; Freeland, J. W.; Preissner, C.; Hla, S.-W. *Adv. Funct. Mater.* **2013**, *23*, 2646–2652.
- (22) Chiu, C.-Y.; Chan, Y.-L.; Hsu, Y. J.; Wie, D. H. *Appl. Phys. Lett.* **2008**, *92*, 103101.
- (23) Rose, V.; Freeland, J. W.; Gray, K. E.; Streiffer, S. K. *Appl. Phys. Lett.* **2008**, *92*, 193510.

- (24) Akiyama, K.; Eguchi, T.; An, T.; Hasegawa, Y.; Okuda, T.; Harasawa, A.; Kinoshita, T. *Rev. Sci. Instrum.* **2005**, *76*, 083711.
- (25) Saito, A.; Takahashi, K.; Takagi, Y.; Nakamatsu, K.; Hanai, K.; Tanaka, Y.; Miwa, D.; Akai-kasaya, M.; Shin, S.; Matsui, S.; Ishikawa, T.; Kuwahara, Y.; Aono, M. *Surf. Sci.* **2007**, *601*, 5294–5299.
- (26) Rose, V.; Chien, T. Y.; Hiller, J.; Rosenmann, D.; Winarski, R. P. *Appl. Phys. Lett.* **2011**, *99*, 173102.
- (27) Wang, K.; Rosenmann, D.; Holt, M.; Winarski, R.; Hla, S.-W.; Rose, V. *Rev. Sci. Instrum.* **2013**, *84*, 063704.
- (28) Bancroft, G. M.; Gudat, W.; Eastman, D. E. *Phys. Rev. B* **1978**, *17*, 4499–4504.
- (29) Pons, S.; Mallet, P.; Veuillen, J.-Y. *Phys. Rev. B* **2001**, *64*, 193408.